Characterization of Yb:YAG active slab media based on a layered structure with different doping

A.Lapucci*[a], M.Ciofini [a], L.Esposito[b], P.Ferrara[c],L.A.Gizzi[c], J.Hostaša[b,e], L.Labate[c], A.Pirri[d], G.Toci[d], M.Vannini[d]

[a] C.N.R. - National Research Council, Istituto Nazionale di Ottica (CNR-INO), Largo Enrico Fermi 6, I-50125 Firenze, Italy; [b] C.N.R. - National Research Council, Institute of Science and Technology for Ceramics (CNR-ISTEC), Via Granarolo 64, 48018 Faenza, Italy; [c] C.N.R. - National Research Council, Istituto Nazionale di Ottica (CNR-INO), Via G. Moruzzi, 1 - I-56124 Pisa, Italy; [d] C.N.R. - National Research Council, Institute of Applied Physics "Carrara" (CNR-IFAC), Via Madonna del Piano 10, I-50019 Sesto Fiorentino (FI) Italy; [e] Department of Glass and Ceramics, ICT Prague, Technická 5, 166 28 Prague, Czech Republic

ABSTRACT

Slabs with non-uniform doping distribution are studied with the aim of reducing thermal deformations in high-energy high-average-power Yb:YAG slab systems. We present a numerical analysis based on Finite Element Mesh (FEM) methods suitable to model non-uniform devices. The thermal variation of the refractive index, the end-faces deformations and the photo-elastic effect have been calculated in order to estimate the total thermal-lens effect. The stress distributions are also obtained. Some results of this numerical approach are compared to experimental thermal lens measurements in a simple geometry for both uniform and structured samples, in order to validate the numerical procedures. Finally we compare numerical simulations for different single- or double-sided pumping and cooling geometries. They show that structured slabs can reduce thermal gradients with respect to uniformly doped means with comparable absorption and geometry. This means a reduction of thermal lens effect and thus an increase of maximum allowed pump power loading. Previous literature reports some work made with structured slabs where higher doping was located in layers with lower pump radiation levels, in order to get a more uniform absorption. Interestingly our modeling indicates that reduced thermal effects are instead obtained when a higher doping is located close to the cooled surfaces.

Keywords: Yb:YAG Lasers, High Energy Lasers, Slab lasers, Ceramic lasers

1. INTRODUCTION

Ytterbium doped YAG materials are the chief candidates for the attainment of High Energy Diode Pumped Solid State Laser (DPSSL) systems working in high rep. rate pulsed regimes [1]. YAG ceramics have already proven their advantages over single crystals for high average power systems, both in terms of higher fracture limit levels and in terms of ease of production. The ceramic sintering process has also the advantage of allowing the production of "structured active media", namely samples consisting of several volumes with different doping levels. Recently structured slabs have been obtained in YAG ceramics shaped from a stack of differently doped layers [2-4]. In this work the ceramic material is prepared by stacking differently Yb-doped layers through cold isostatic pressing. Calcination, reaction sintering, annealing and polishing processes complete the slab production.The details of the production process have been reported elsewhere [5]. The optimization of the doping distribution is strongly related to the pumping and cooling geometry of the active medium and a complex numerical analysis is needed to assess the advantages or disadvantages of a specific design in terms of thermal deformation and fracture limit of the active medium. In many classical cases, such as those of uniform cylindrical rods or uniform disk lasers, symmetry considerations help in simplifying the numerical approach.

antonio.lapucci@ino.it; phone +39.055.2308226; fax +39.055.2337755

High-Power, High-Energy, and High-Intensity Laser Technology; and Research Using Extreme Light: Entering New Frontiers with Petawatt-Class Lasers, edited by Joachim Hein, Georg Korn, Luis Oliveira Silva, Proc. of SPIE Vol. 8780, 87800J

In this paper we present a thermo-mechanical modeling based on Finite Element Mesh (FEM) methods suitable to model non-uniform devices. We firstly show some results of this approach applied to a simple geometry that we can test experimentally. The measurements of thermal lens effective focal lengths (e.f.l.s) are reported for both uniform and structured samples in order to validate the numerical approach. Finally we compare numerical simulations for different single- or double-sided pumping and cooling geometries. They show that structured slabs can reduce thermal gradients with respect to the uniformly doped means with comparable absorption and geometry. This means a reduction of thermal lens effect and thus an increase of maximum allowed pump power loading. Previous literature reports structured slabs usually with higher doping located in layers where a lower pump radiation level is present, in order to get a more uniform power absorption [2,3]. Interestingly our modeling indicates that reduced thermal effects are instead obtained locating higher doping levels close to the cooled surfaces.

2. NUMERICAL F.E.M. ANALYSIS

2.1 Three dimensional numerical simulation approach

Several papers on solid state lasers dealt with the thermal analysis in the past [6-8]. They all end with the conclusion that the optical path difference at different transverse positions is related to three contributions. The refractive index variations with temperature, the surface bending due to thermal expansion and the stress induced birefringence due to the photo-elastic effect.

$$OPD(r) = \left(\int_0^d \frac{dn}{dT} \cdot \Delta T(r,z) dz \right) + n_0 \cdot \Delta u(r) + \left(\sum_{i,j=1}^{3} \int_0^d \frac{\partial n}{\partial \varepsilon_{ij}} \cdot \varepsilon_{ij}(r) dz \right) \quad (1)$$

Where d is the sample thickness , n_0 is the refractive index without deformations, Δu(r) is the surface deformation at radial position r, and ε_{ij} is the strain tensor. In what follows z is the direction parallel to the cylindrical axis and to the "optical rays propagation" . Variables (x,y) or (r,Φ) describe a cartesian or polar coordinate system in the planes transverse to propagation.

Our approach is based on the adoption of a commercial F.E.M. (Finite Element Mesh Calculation Method) software package [9] to obtain the thermal and mechanical behavior of our structured samples, given the heat loading distribution and thermal boundary conditions. The software package output consists in a scalar temperature variation field $\Delta T = T - T_{REF}$, the geometrical displacements of each node of the mesh and, finally, the 6 components of the stress tensor (σ_i and τ_{ij}). Strains can be easily calculated from the stress and temperatures fields using the conventional linear elasticity equations:

$$\begin{cases} \varepsilon_r = \frac{1}{E}\left[\sigma_r - \nu\left(\sigma_\phi + \sigma_z\right)\right] + \alpha\left(T - T_{REF}\right) \\ \varepsilon_\phi = \frac{1}{E}\left[\sigma_\phi - \nu\left(\sigma_r + \sigma_z\right)\right] + \alpha\left(T - T_{REF}\right) \\ \varepsilon_z = \frac{1}{E}\left[\sigma_z - \nu\left(\sigma_\phi + \sigma_r\right)\right] + \alpha\left(T - T_{REF}\right) \end{cases}$$

. (2)

$$\begin{cases} \gamma_{r\phi} = 2\left(\frac{1+\nu}{E}\right)\tau_{r\phi} = 2\varepsilon_{r\phi} \\ \gamma_{rz} = 2\left(\frac{1+\nu}{E}\right)\tau_{rz} = 2\varepsilon_{rz} \\ \gamma_{\phi z} = 2\left(\frac{1+\nu}{E}\right)\tau_{\phi z} = 2\varepsilon_{\phi z} \end{cases}$$

Where, considering our host material (YAG), we have that $E = 2.8\ 10^{11}\ Pa$ is the Young modulus, $\nu = 0.28$ the Poisson coefficient , $\alpha = 7.9\ 10^{-6}\ °C^{-1}$ the thermal expansion coefficient and $T_{REF} = 20°C$ the reference temperature, that is the temperature of the cooling system.

The first two contributions to the OPD are directly calculated from the output of the thermo-mechanical software package. To determine the third contribution we need the relation between the refractive index (for the different polarization directions) and the strain tensor. This relation is in general expressed by a variation of the dielectric impermeability 2nd rank tensor B_{ij} [7] and is given by the set of equations:

$$\Delta B_{ij} = p_{ijkl}\,\varepsilon_{kl} \tag{3}$$

$$\Delta n_i = -\frac{n_0^3}{2}\cdot \Delta B_{ii}^{*} \tag{4}$$

Where p_{ijkl} is the 4th rank elasto-optical tensor, n_i are the refractive indices along the principal axes of the stress-perturbed indicatrix [6] and ΔB_{ij}^{*} is the diagonalized dielectric impermeability variation tensor. Fortunately equation (3) reduces to a much simpler formulation in case of a cubic crystal with [111] orientation [7]. Moreover Khazanov [8] demonstrated that the YAG ceramic behavior is similar to that of the [111] oriented single crystal, given the averaging effect of the different grains orientations. This fact was also confirmed by experimental birefringence measurements in Nd:YAG ceramics [10]. Under these conditions the elasto-optical tensor simplifies to the form:

$$\overline{\overline{\Delta B}}(x',y',z') = \begin{vmatrix} p_{11}\varepsilon_1 + p_{12}(\varepsilon_2+\varepsilon_3) & p_{44}\varepsilon_6 & p_{44}\varepsilon_5 \\ p_{44}\varepsilon_6 & p_{11}\varepsilon_2 + p_{12}(\varepsilon_1+\varepsilon_3) & p_{44}\varepsilon_4 \\ p_{44}\varepsilon_5 & p_{44}\varepsilon_4 & p_{11}\varepsilon_3 + p_{12}(\varepsilon_1+\varepsilon_2) \end{vmatrix} \tag{5}$$

with p_{11}= - 0.0290 , p_{12}= 0.0091 , p_{44}= - 0.0615.

Now it is important to note that previous literature has always looked for an analytical solution for the strains and thus it has mainly treated "rod like" cases [6] (also referred to as "plain strain approximation" [7]) or "disk like" cases [11] ("plain stress approximation") in which a two-dimensional approach can be adopted either because of the reduced thickness or because of a translationally invariant cylindrical symmetry. In order to maintain the features of our structured samples (see Fig.1), translational invariance along z cannot be claimed and a complete 3D approach is to be adopted. We thus performed the B-matrix elements calculation from the output of our software package, on two selected "ray paths" (parallel to the z axis), one on the axis of the cylindrical pumped volume and one on the lateral surface of that same volume. Transverse refractive indices $n_r(k)$ and $n_\Phi(k)$ (with respect to the z-propagating waves) have been obtained through a diagonalization of the complete B matrix on each node (k) of the model mesh belonging to the two selected paths. The details of this calculation procedure will be reported elsewhere [12]. In order to account for the unpolarized thermal lens effect, the refractive indices n_r and n_Φ have been averaged and the Optical Path Difference between axial and boundary paths of the pumped region has been used as wave-front curvature sag.

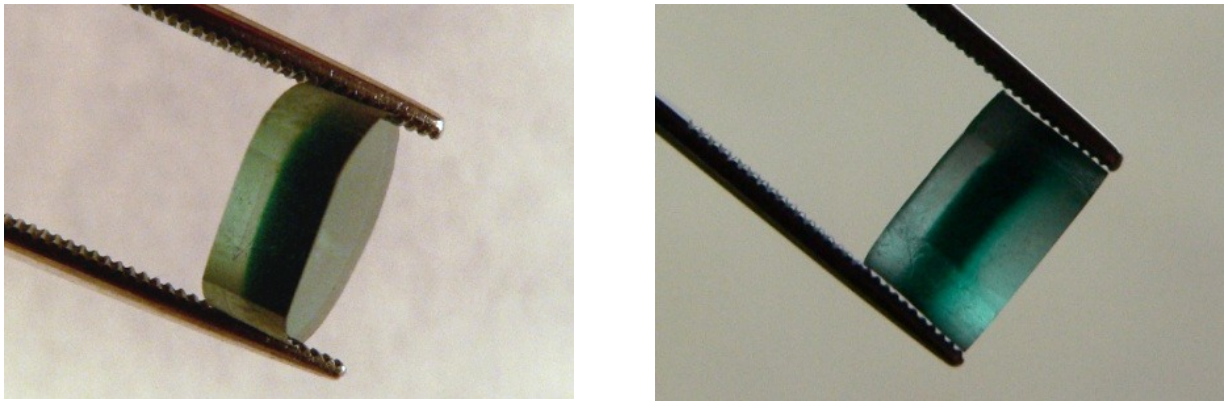

Figure 1. Portraits of two layered structure samples described in this work.

2.2 Numerical results for the one-sided sample geometry

In this paragraph we show the results obtained from our numerical approach for five sample cases of Yb:YAG pellets representative of the real devices available in our labs (Fig.1) and whose experimental behavior is described in the following section of this paper. To simplify the numerical modeling we unified the geometry of the five samples. All the pellets are considered to be cylindrical with a 10 mm diameter and 3 mm thickness. They are pumped on a 0.5 mm diameter area on one side and cooled on the ring surface external to a 5 mm diameter on the other side. This geometrical model represents the active medium mounting shown in Fig.6 of next section. 3D example plots of our software package calculations are shown in Fig.2.

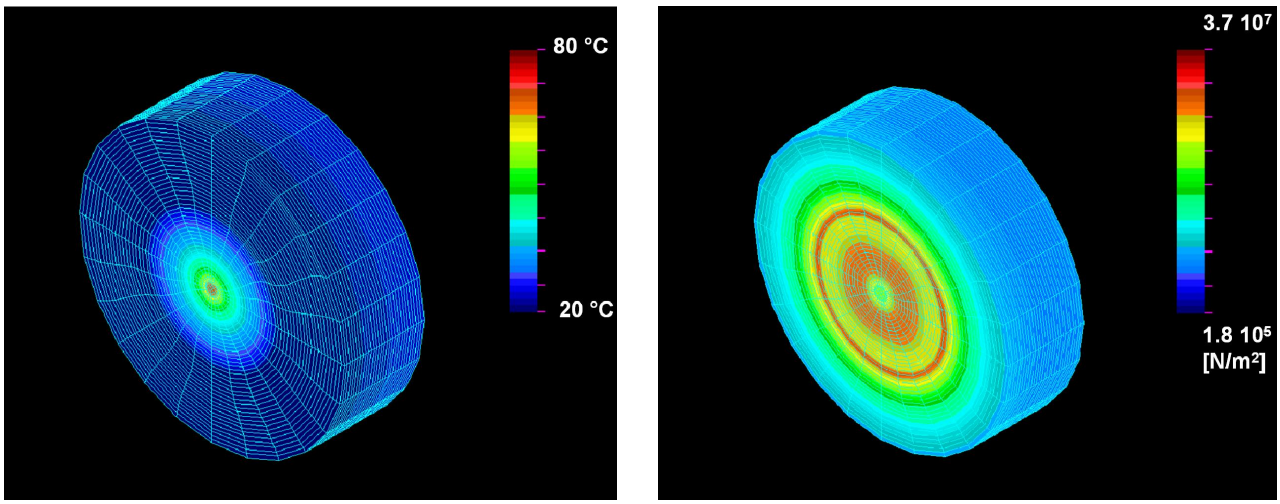

Figure 2. Examples of three dimensional plots of the FEM software output: Temperatures (Left) and Von Mises Stress (Right)

The pellets are modeled as a stack of 5 layers all with 0.6 mm thickness. Thus in our numerical simulations the five samples, with different structure, differ only in the thermal load input distributions. Such distributions are a function of the pump radiation absorption and thus of the doping level of each layer. The total thermal load is equal to 2.5 W for all the five samples. Table 1 reports the doping levels adopted in our simulations to represent a series of graded-doping or stepped-doping devices presently under test in our laboratories. The first doping value refers to the layer on the pumped side of the sample, while the last one refers to the layer on the cooled side.

Table 1. Doping levels of the uniform/structured samples studied in our numerical simulations.

Sample #	Doping Distribution	Doping levels
1	*Uniform*	5%
2	*Graded*	(3,3,5,5,7)%
3	*Graded*	(1,3,5,7,7)%
4	*Stepped*	(0,0,10,10,10)%
5	*Capped*	(0,10,10,10,0)%

Fig.3 reports the thermal distributions on an *r-z* section of the cylindrical pellet obtained from our simulations for the five samples defined in Table 1. In the figure, cooled sides are on the left and pumped sides are on the right for all the samples, and sample-sections are plotted with reference to sample number 1 to 5 from the left-hand to the right-hand side.

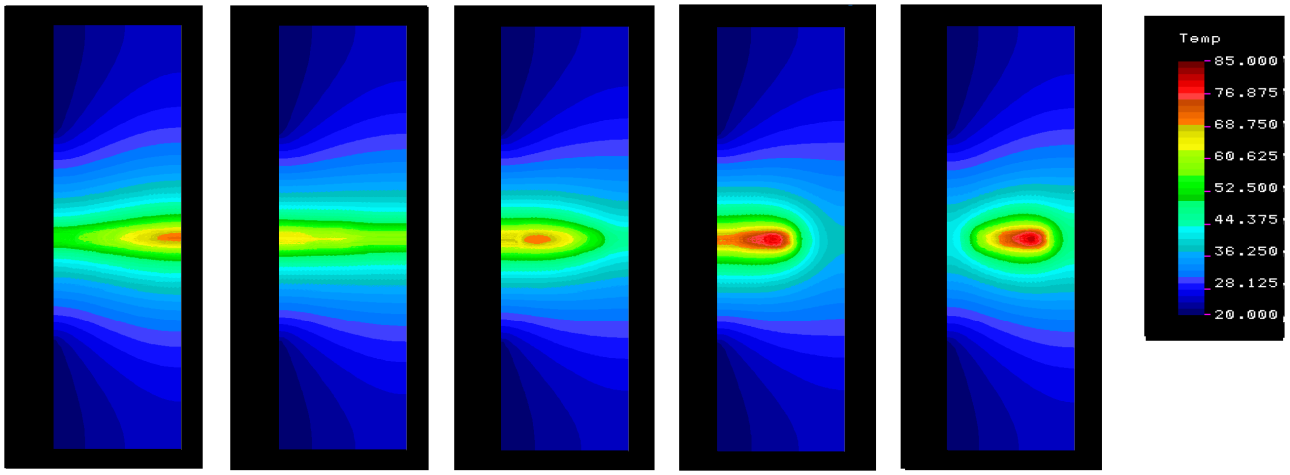

Figure 3. Temperature distributions for the five studied samples (samples 1 to 5 from left to right). Plots represent a radial section of the cylindrical samples (cooling surface on the left, pumping beam entering from the right).

Interestingly from these data we can see that graded doping (see the second plot in Fig.3) can make the absorption of the pump radiation more uniform than all the other cases, including the case of uniform doping. Consistently the maximum internal temperature also results reduced. Maximum temperatures are for the five samples $T_{max}(1)=71°C$, $T_{max}(2)=65°C$, $T_{max}(3)=71°C$, $T_{max}(1)=81°C$, $T_{max}(1)=81°C$. We will see that, in our case, this will not mean a reduction in the thermal lens related to the temperature dependent refractive index variation, that is the first term of eq.(1). This is due to the fact that our geometry (the ring shaped cooler) produces a substantially radial heat flow. The z-oriented beam propagation determines an averaging of the refractive index variation almost cancelling the advantages of more uniform pump power absorption. We will see in section 4 that this is not the case of systems with longitudinal heat flow.

Fig.4 shows the pellet deformations in the five analyzed cases. For the sake of generality and simplicity, mechanical constraints due to the sample brazing on the cooler are considered weak in this set of numerical simulations. Thus the center of the pumped face is the only point that is considered fixed. Here it is clear that lower surface modifications are obtained with samples with low doping close to the external surfaces (cases 4 and 5). The surface sags for the five cases are listed in Table 2.

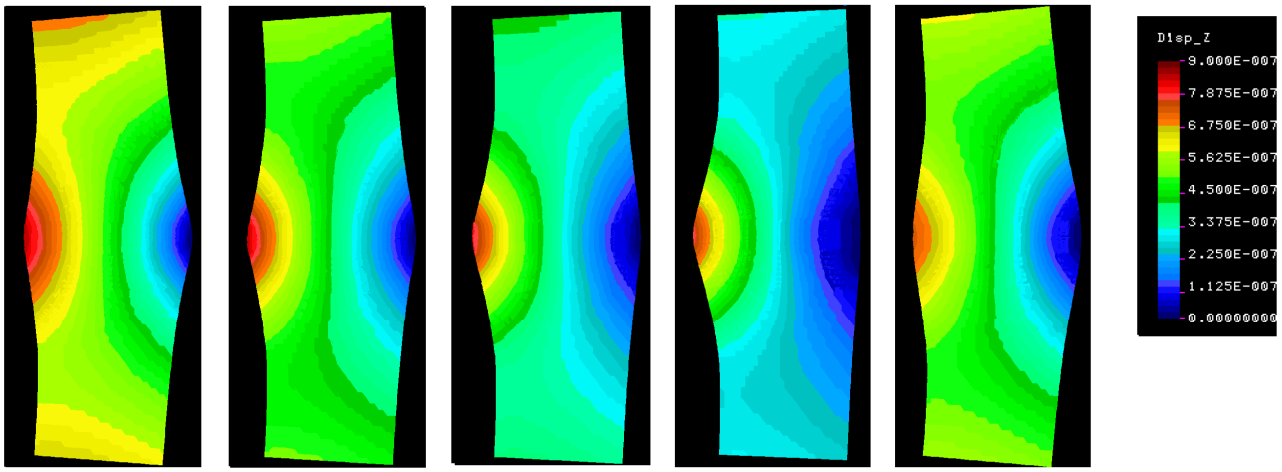

Figure 4. Deformation patterns for the five studied samples (samples 1 to 5 from left to right). Plots represent a radial section of the cylindrical samples (cooling surface on the left, pumping beam entering from the right).

Table 2. Surface sags for the five analyzed cases.

Sample #	Δu_p (pump side)	Δu_c (cooler side)
1	$3.567\ 10^{-8}$ m	$1.940\ 10^{-8}$ m
2	$2.476\ 10^{-8}$ m	$2.980\ 10^{-8}$ m
3	$1.295\ 10^{-8}$ m	$3.200\ 10^{-8}$ m
4	$0.467\ 10^{-8}$ m	$3.420\ 10^{-8}$ m
5	$1.315\ 10^{-8}$ m	$0.720\ 10^{-8}$ m

Fig.5 shows the von Mises stress value for the five cases analyzed in this paragraph. Here it is clear that the "stepped" and "capped" cases that show an advantage in terms of surface deformations, present higher internal stresses. This because a higher doping has been used in the internal layers, in order to reach the same total pump absorption. Maximum Von Mises stress results for the five cases: $\sigma_{VM}(1)= 3.057\ 10^7$ N/m^2, $\sigma_{VM}(2)= 2.934\ 10^7$ N/m^2, $\sigma_{VM}(3)= 3.337\ 10^7$ N/m^2, $\sigma_{VM}(4)= 3.721\ 10^7$ N/m^2, $\sigma_{VM}(5)= 3.604\ 10^7$ N/m^2. This means that the graded sample (number 2) is expected to show the highest fracture limit while the stepped sample is expected to show the lowest. Even though differences between best and worst case are of the order of 25% in our case study.

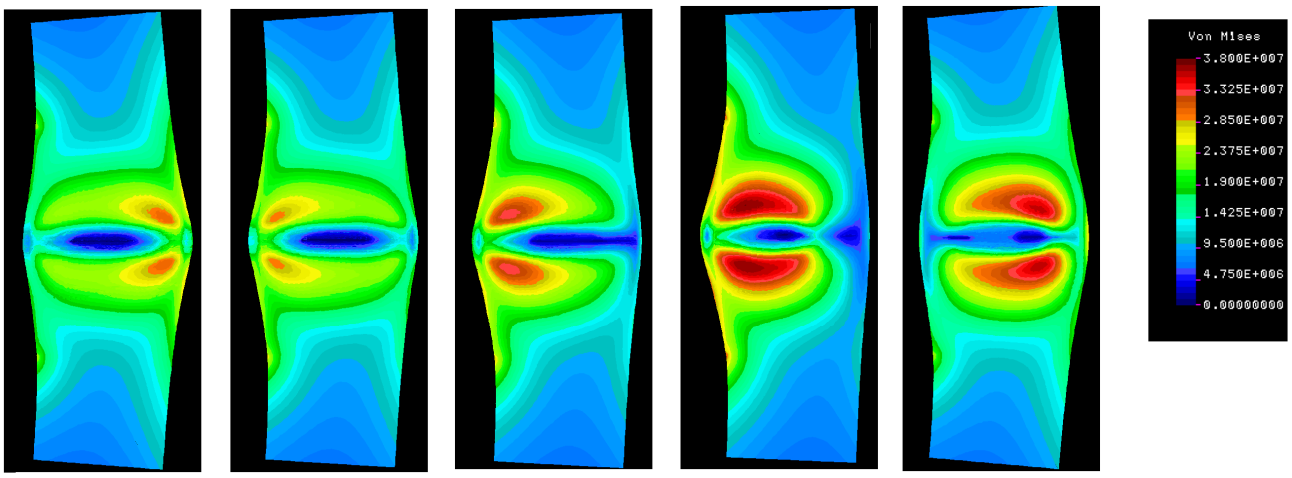

Figure 5. Von Mises stress distributions for the five studied samples (samples 1 to 5 from left to right). Plots represent a radial section of the cylindrical samples (cooling surface on the left, pumping beam entering from the right).

Finally Table 3 reports the thermal lens contributions, according to equation 1, obtained from the FEM analysis and the post processing described in the previous paragraph for the photo-elastic effect. We have to note that we adopted the same criterion indicated in [7] to account for the direct temperature dependence of the refractive index. That is to say that we considered the dn/dt to be adopted in eq.(1) as a partial derivative of the refractive index at constant strain (i.e. $(\partial n/\partial T)_\varepsilon$). This is in fact higher than the coefficient experimentally measured on crystals or ceramics ($\sim 7.3\ 10^{-6}$ °C^{-1} see [13]) that can be regarded as a partial derivative at constant stress (i.e. $(\partial n/\partial T)_\sigma$). Following the calculations reported in [7] we have adopted a coefficient $(\partial n/\partial T)_\varepsilon = 16.0\ 10^{-6}$ °C^{-1}, and we will see that it gives thermal lens values in good quantitative agreement with the experimental measurements reported in the next section.

Table 3. Thermal lens contributions and e.f.l. for the five analyzed samples, under a thermal power loading equal to 2.5 W.

Sample	F (dn/dT) [cm]	F (surface) [cm]	F(ε_{ij}) [cm]	**e.f.l.(F_{Tot}) [cm]**
1	9.72	70.90	202.74	***8.20***
2	9.86	71.60	231.26	***8.35***
3	9.95	86.90	202.74	***8.55***
4	9.81	100.00	190.96	***8.53***
5	9.99	192.00	127.1	***8.84***

Observing Table 3 we immediately see that the effect of the structured layers on the total thermal lens is almost negligible. As pointed out previously this is related to a substantially radial (thus transverse) heat flow direction and a longitudinal layer structure. This particular geometry produces this specific result. We will see in section 4 that different overall results are obtained with different pumping and cooling geometries. We performed these case study simulations in order to compare them with the experimental set-up available un our labs, and thus to validate the numerical simulation procedure. We would also like to comment here that our numerical analysis produces lower thermal lens contributions from surface deformations in the case of the stepped and capped samples, but a higher photo-elastic contribution. This latter is a feature that doesn't come out if the modeling is performed in the "plain strain approximation" [11], that would consider stresses as the mean value integrated along the whole thickness of the pellet [7].

3. EXPERIMENTAL THERMAL LENS MEASUREMENTS

The validation of our numerical simulation is obtained by means of experimental measurements of thermal lensing performed on both the uniform and structured samples already available in our labs. The layer thicknesses and doping levels of the tested samples are summarized in Table 4.

Table 4. Layer thickness and doping of the experimentally available samples.

Sample	Distribution (Material)	Doping levels	Layer Thickness [mm]
A	*Uniform (Ceramic)*	10 %	1.25
B	*Uniform (Crystal)*	8%	2
C	*Stepped (Ceramic)*	(0,10,0)%	(0.6-1.2-0.6)
D	*Capped (ceramic)*	(0,10)%	(1.6-2.0)

The thermal lens effect in the different samples was characterized using the setup described in Figures 6 and 7. The experiment was designed to allow the comparison of the thermal lens effect both on lasing and non lasing samples, in order to show possible differences in the thermal load. For this purpose the samples are inserted in a longitudinally pumped laser cavity, and a probe beam is used to measure the thermal lens effect. The pump source is a fiber coupled semiconductor laser emitting at 936 nm. The output from the fiber (200 μm diameter, 0.22 NA) is refocused and magnified by a pair of achromatic doublets on a waist with 500 μm diameter @$1/e^2$ located in the center of the sample. A maximum incident pump power of 21.8 W CW was used in the experiments. The pump beam emerging from the refocusing optics is steered by the dichroic mirror DM and is then injected into the laser cavity through the end mirror EM (dichroic, high transmission at the pump wavelength, high reflection at the laser wavelength). The cavity is folded with the flat mirror M_1 and with the spherical mirror M_2 (focal length 100 mm), and it is closed by the output coupler OC. The overall distance between M_2 and EM is 113 mm, and the distance between M_2 and OC is 210 mm. This results in a fundamental mode cavity radius of 100 μm for the "cold" cavity, on the waist located at the mirror EM. The samples are brazed with Indium on a copper heat sink with a central circular aperture having a diameter of 2.5 mm. The cooling occurs on the opposite side with respect to incidence of the pump beam.

The thermal lens is measured by means of a probe beam emitted by a HeNe laser. The beam is expanded and collimated, sent into the sample collinearly with the pump beam and the cavity laser beam through the mirrors DM and EM, and extracted from the cavity through the mirror M_1. The probe beam illuminates the whole clear aperture of the sample holder. The wavefront distortion induced by thermal effects is measured by means of a Shack-Hartmann wavefront sensor (model ML4010 by Metrolux GmbH) with a sensing area of 8.98 x 6.71 mm^2 and 200 μm pitch of the microlenses array. In order to measure the wavefront distortion occurring over an area of about 500 μm diameter, the probe beam was expanded by an afocal telescope formed by the two positive lenses L_1 and L_2 with nominal focal lengths f_1=155 mm and f_2=750 mm placed at a distance $d=f_1+f_2$ (see Fig. 7). The sample and the sensor are placed in the conjugate planes of the telescope, i.e. at f_1 from L_1 and at f_2 from L_2 respectively. The probe beam at the output of the sample is then reimaged on the sensor with a magnification $M=f_2/f_1$, without any further curvature introduced by the telescope [14]. The magnification of the telescope was accurately measured and it resulted M=4.81. Several filters (F1, F2, F3) are used to reject the residual pump beam that would otherwise impinge on the sensor.

The thermal deformation of the wavefront is usually measured at several levels of incident pump power. In order to compensate for the distortion introduced by the various elements on the optical path, the wavefront is acquired in "cold" conditions (i.e. for zero incident pump power) and then subtracted from the measurements obtained with the pump beam on. An example of an acquired wavefront is shown in Figure 7. A circular portion of the wavefront with radius a corresponding to the pumped area of the sample is then selected and analyzed by fitting with Zernike polynomials up to the 6th order. The effective dioptric power D_{th} of the thermal lens is then calculated with the formula

$$D_{th} = \frac{1}{f_{th}} = \frac{4Z_{2,0}}{a^2} M^2 \tag{6}$$

where $Z_{2,0}$ is the coefficient of the Zernike polynomial with radial index 2 and azimuthal index 0, corresponding to the wavefront defocus. In these measurements, we adopted a value of a=1.2 mm (on the sensor plane), corresponding to the pump beam radius @ $1/e^2$ (250 μm) on the sample plane.

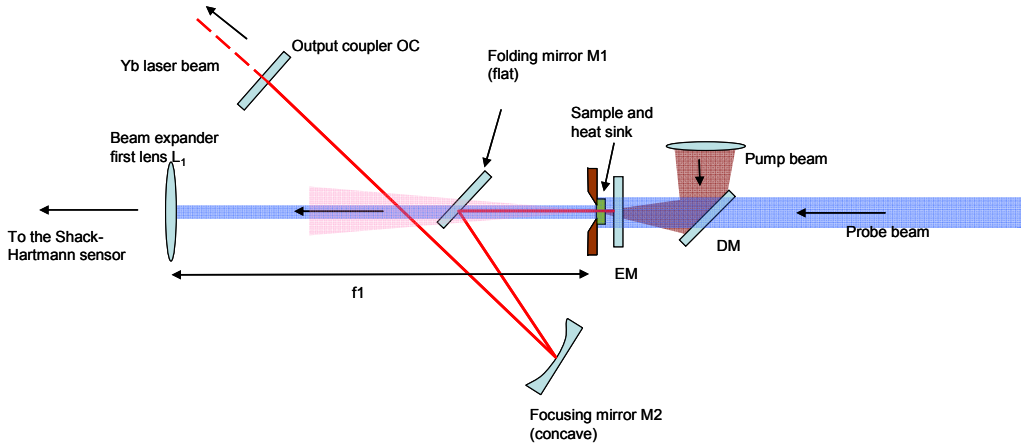

Figure 6. Experimental set up for the testing of structured samples (see also Figure 7).

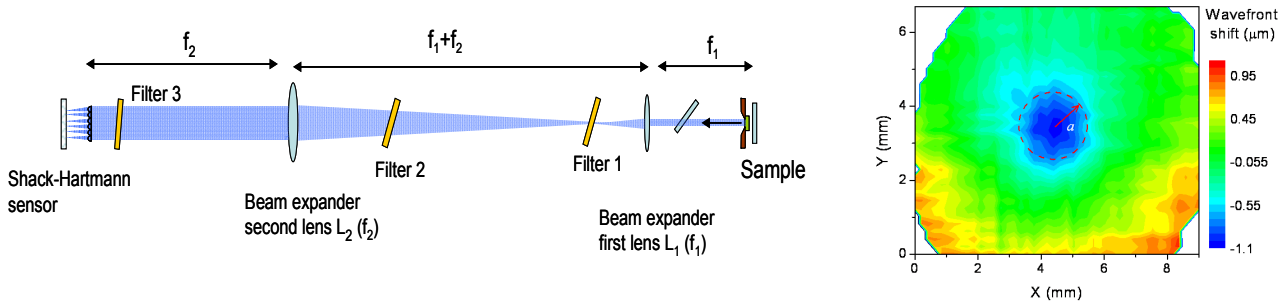

Figure 7. Left - Setup for the measurement of the wavefront thermal distortion and of the thermal lens dioptric power. Right - Map of the wavefront thermal aberration as recorded by the Shack-Hartmann sensor; the limiting aperture for the Zernike polynomial fitting and for the measurement of the wavefront curvature is also shown.

Due to the different absorption featured by the various samples, the dioptric power of the thermal lens was analyzed as a function of the absorbed pump power. An example of this analysis is reported in Figure 8, which shows the behavior of the thermal lens dioptric power for different absorbed power levels. It can be visible that the thermal lens dioptric power scales linearly with to the absorbed pump power.

The lasing condition for the sample in Figure 8 was obtained with an output coupler with 2% transmission. Usually, an OC with low transmission was used in the measurement, in order to maximize the intracavity circulating power and thus the difference in thermal load between lasing conditions and non lasing conditions. A small difference in the thermal lens occurs between lasing and non lasing conditions, due both to the different thermal load and to the different geometry of the heat source occurring in the two conditions. A more detailed description of the thermal lens evaluation and its dependence on the analyzed beam aperture is given elsewhere [15].

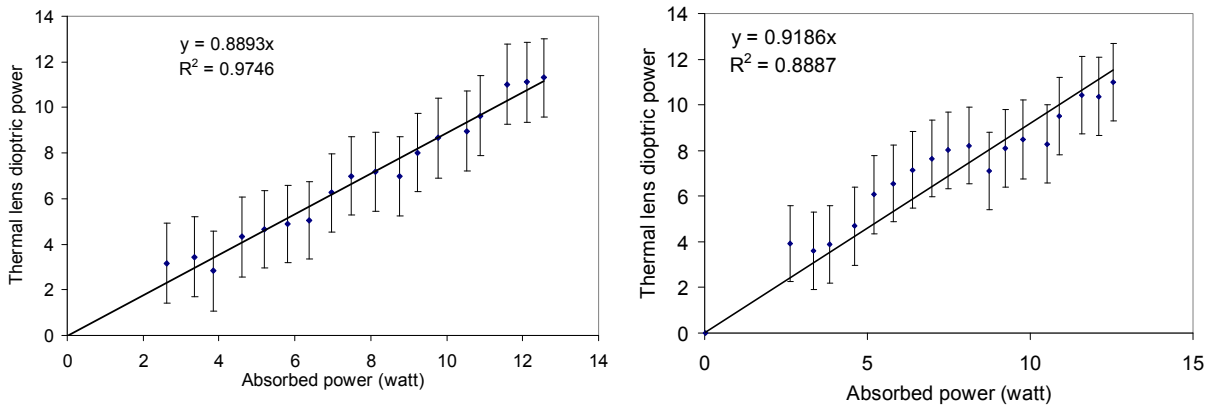

Figure 8. Thermal lens dioptric power as a function of absorbed power in the case of the uniform doping ceramic (sample A in table 4), with (left) and without (right) laser action. The expression in the graphs are respectively the best linear fit and the correlation coefficient.

As can be seen from the measures reported in Fig.8 the thermal lens dioptric power scales linearly with the absorbed power. The linear coefficient *C* is reported in Table 5, obtained from the 4 measured samples in lasing and non-lasing conditions.

Table 5. Thermal lens dioptric power Coefficient C (dioptric power per Watt of pump radiation absorption).

Sample	*C (Laser on)*	*C (Laser off)*
A	0.889	0.919
B	0.959	0.988
C	0.870	1.003
D	1.138	1.166

The experimental tests performed on the structured ceramic samples available so far, substantially confirm the predictions of our numerical analysis. Thermal lens measurements reveal very little differences between different samples. The effective focal length values measured for absorbed powers of the order of 17-18 W corresponding to a thermal load comparable to that adopted in our simulations are in the range 5 to 7 cm. These values are obtained considering 14% of the absorbed power lost as heat. Indeed, in real samples, the pump quantum efficiency is lower than that theoretically expected due to defects in the active sites producing non-radiative decays. This fact also determines a higher thermal loading fraction [16]. Experimental data indicate a fractional thermal loading between 0.12 and 0.15 for 8-10% doped Yb:YAG samples. The measured effective focal length values compare well with the numerical calculations. This can be considered a satisfactory validation of our numerical procedure and allows us to use it to model different geometries and various doping distributions as will be illustrated in the following section for a second case study.

4. ADVANTAGEOUS GEOMETRIES FOR STRUCTURED MATERIALS

In this section we present the results of a second set of numerical simulations. We performed this new analysis to study the behavior of active media with a geometry more similar to that of high energy pulsed Yb:YAG laser systems [17,18]. In this second case we study again cylindrical pellets with a thickness of 2 mm. The pumped volume consists in a central cylinder with 0.8 mm diameter and pump radiation is input from either sides of the pellet. Cooling is performed on the entire surface of the pumped faces as it happens in systems with cooling fluid flows [17,18] or contact with highly conductive transparent coolers [19]. In this case the heat flow is no longer mainly transverse as in the case described in the previous sections. As a consequence longitudinal variations in the power absorption distributions, produced by the differently doped layered structures, turn out to produce different thermal lens focal lengths. Again, for simplicity of calculations, we have analyzed samples with the same number (5) of equally thick layers (0.4 mm). A uniform sample is compared to two others with different graded doping distribution. The first one has higher doping levels concentrated on the external layers (thus closer to the cooling surfaces) and the second has higher doping levels concentrated in the internal volume of the pellet as in the cases reported in previous literature [2,3]. The doping distributions adopted in this study are summarized in Table 6. Fig.9 shows the temperature distributions in an *r-z* section of the pellet for the three differently doped cases. Again, doping and input power have been chosen in such a way that all the samples absorb the same amount of power.

Table 6. Doping levels of the uniform/graded samples studied in this second set of numerical simulations.

Sample	Distribution	Doping levels
I	*Uniform*	5%
II	*Graded* *"External-doping"*	(7,5,1,5,7)%
III	*Graded* *"Internal-doping"*	(3,5,7,5,3)%

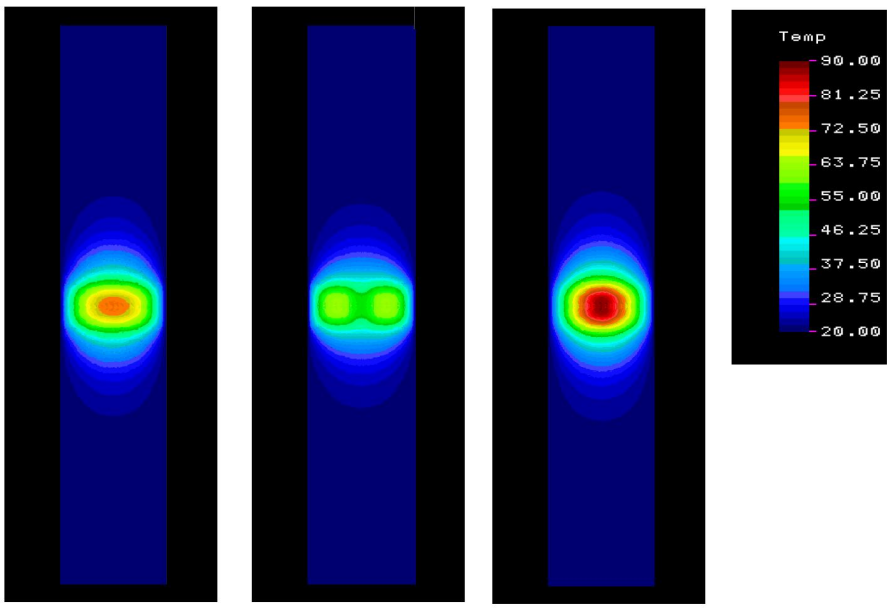

Figure 9. Temperature distributions for the three double-side cases studied in this section.

Table 7 summarizes the results of this study in terms of thermal lens effect. Again with this geometry the thermal lens contribution due to the temperature variation of the refractive index results the most relevant one. We obtain in this case that the graded system with high doping concentrated on the external layers produces a 14% reduction in the thermal lens effect with respect to the uniform case. On the contrary, a graded structure with internally concentrated doping [2,3] results disadvantageous in terms of thermal lens effect.

Table 7. Thermal lens contributions and e.f.l. for the three analyzed samples, under a thermal power loading equal to 5.4W.

Sample	F (dn/dT) [cm]	F (surface) [cm]	F(ε_{ij}) [m]	**e.f.l.(F_{Tot}) [cm]**
I	17.2	96.4	17	***14.5***
II	20.1	95.0	34	***16.5***
III	15.9	99.1	3	***13.1***

5. CONCLUSIONS

In this paper we have summarized our present activity devoted to the characterization of Yb:YAG active slab media, based on a layered structure with different doping. We developed a procedure to analyze numerically the thermo-mechanical behaviour of our samples and to predict their consequent optical properties. These simulations have been compared with a set of experimental results in order to validate the procedure. Furthermore a series of simulations here described enabled us to anticipate some advantages that can be obtained with the adoption of such a kind of engineered active media. These structured ceramics are intended to be applied in the construction of High Energy Diode Pumped Solid State Laser (DPSSL) systems working in high rep-rate pulsed regimes.

We acknowledge support from the EC initiative "LASERLAB-EUROPE" (EC contract no. 284464)Â - Joint Research Activity WP33 - "European Research Objectives on Lasers for Industry, Technology and Energy (EURO-LITE)" and the HiPER (ESFRI-FP7) project. J.H. would also like to acknowledge the financial support from a specific university research grant (MSMT No 20/2013).

REFERENCES

[1] Krupke, W., "Ytterbium solid-state lasers—the first decade", IEEE J. Sel. Top. Quantum Electronics 6, 1287–1296, (2000).

[2] Tang, F., Cao, Y.G., Huang, J.Q., Guo, W., Liu, H.G., Wang, W.C., Huang, Q.F. and Li, J.T., "Diode-pumped multilayer Yb:YAG composite ceramic laser", Laser Phys. Lett. 9, No. 8, 564–569, (2012).

[3] Kamimura, T., Okamoto, T., Aung, Y.L. and Ikesue, A., "Ceramic YAG Composite with Nd Gradient Structure for Homogeneous Absorption of Pump Power", Conference on Lasers and Electro-Optics (CLEO), paper: CThT6, OSA Technical Digest Series (CD) (2007).

[4] Sato,Y., Ikesue, A. and Taira, T., "Tailored Spectral Designing of Layer-by-Layer Type Composite $Nd:Y_3ScAl_4O_{12}/Nd:Y_3Al_5O_{12}$ Ceramics", IEEE J. Sel. Top. Quantum Electronics 13(3), 838-843, (2007).

[5] Esposito, L. , Epicier, T., Serantoni, M., Piancastelli, A., Alderighi, D., Pirri, A., Toci, G., Vannini, M., Anghel, S., and Boulon, G., "Integrated analysis of non-linear loss mechanisms in Yb:YAG ceramics for laser applications", J. Eur. Ceram. Soc., 32(10), 2273-2281, (2012).

[6] Koechner,W. and Rice, D.K., "Effect of birefringence on the performance of linearly polarized YAG:Nd lasers", IEEE J. Quantum Electronics QE-6(9), 557–566, (1990).

[7] Chénais, S., Druon, F., Forget, S., Balembois, F. and Georges, P., "On thermal effects in solid-state lasers: The case of ytterbium-doped materials", Progress in Quantum Electronics 30(4), 89–153, (2006).

[8] Khazanov, E.A., "Thermally induced birefringence in Nd:YAG ceramics",Opt. Lett., 27(9), 716-718, (2002).

[9] COSMOS M, Design Star Product, Structural Research and Analisys Corp. – (User's Guide and Tutorial), www.cosmosm.com , Los Angeles, 2001.

[10] Shoji, I., Sato,Y., Kurimura,S., Lupei, V., Taira, T., Ikesue, A. and Yoshida, K., "Thermal-birefringence-induced depolarization in Nd:YAG ceramics",Opt. Lett. 27(4),234-236 ,(2002).

[11] Cousins, A., "Temperature and termal stress scaling in finite-length end-pumped laser rods", IEEE J. Quantum Electronics QE-28(4), 1057–1069, (1992).

[12] Ferrara, P., et al. "FEM numerical analysis of the thermal lens and birefringence of Yb:YAG ceramic samples with structured geometry", to be published.

[13] Koechner,W. , "Solid-State Laser Engineering" 5th ed., Springer-Verlag, Berlin-Heidelberg, 48-53, (1999)

[14] Chénais S., Balembois F., Druon F., Lucas-Leclin G. and Georges P., "Thermal Lensing in Diode-Pumped Ytterbium Lasers—Part I: Theoretical Analysis and Wavefront Measurements", IEEE J. Quantum Electronics QE-40 (9), 1217-1234, (2004).

[15] Toci, G., et al. " Experimental measurement of the thermal lens effect in Yb:YAG ceramics with layered structure", to be published.

[16] Fan,T.Y., "Heat generation in Nd: YAG and Yb: YAG", IEEE J. Quantum Electronics QE-29(6), 1457–1459, (1993).

[17] Bayramian,A. J., " The Mercury Project: A High Average Power, Gas-Cooled Laser with Frequency Conversion and Wavefront Correction," in Advanced Solid-State Photonics, Technical Digest (O.S.A.), paper MA4,(2006).

[18] Hein, J., Podleska, S., Siebold, M., Hellwing, M., Boedefeld, R., Sauerbrey, R., Ehrt, D. and Wintzer, W., "Diode-pumped chirped pulse amplification to the joule level", Appl. Phys. B 79, 419–422, (2004).

[19] Chou, H.P., Wang, Y.L. and Hasson, V., "Compact and efficient DPSS laser using diamond-cooled technology", Proc. SPIE 5448, 550-560, (2004).